OXFORD JOURNAL
OF STUDENT
SCHOLARSHIP

Restoring Quantum Signal Fidelity Under Decoherence: Echo Pulse Optimization and Relevance to MRI, Brain Tumor Classification, and Neurodiagnostic Accuracy

Eli Kim
eli.kd19@gmail.com

ABSTRACT

Decoherence is the primary obstacle separating today's noisy quantum devices from fault-tolerant quantum computers. When a qubit loses coherence, the quantum information it carries degrades and cannot be recovered. In applications such as MRI signal processing or quantum-assisted brain tumor classification, this loss can translate into diagnostic error. This study uses quantum circuit simulation to evaluate four echo-based dynamical decoupling pulse sequences as software methods for reducing decoherence in single-qubit systems. All simulations were implemented in Python 3.10 using Qiskit and modeled quantum states with density matrices. Monte Carlo analysis was conducted across 100 trials of 1,024 shots per trial to capture realistic measurement noise. The qubit was initialized in superposition and subjected to three noise types: low-frequency phase noise (T_2), high-frequency phase noise, and combined noise ($T_1 + T_2$). These noise types correspond to the relaxation processes that govern MRI signal quality. The four strategies tested were: an unprotected baseline, Hahn Echo, Carr-Purcell-Meiboom-Gill (CPMG), and a Mixed-Sync method. Under low-frequency noise, Hahn Echo restored fidelity to 100.00% from a baseline of 57.90%. Under high-frequency noise, CPMG recovered fidelity to 97.62% from 2.45%. Under combined $T_1 + T_2$ noise, Mixed-Sync improved fidelity only to 65.34% from 60.95%, demonstrating that T_1 energy relaxation causes irreversible loss that pulse sequences cannot overcome. These results are analogous to the T_1-limited signal ceiling in MRI and illuminate fundamental constraints relevant to quantum-assisted neuroimaging.

INTRODUCTION

Quantum computers process information using quantum bits (qubits) that can exist in superposition and become entangled with one another, enabling certain algorithms to explore exponentially large solution spaces more efficiently than classical computers (Nielsen & Chuang, 2009; Preskill, 2018). This capability has generated interest in medical applications: quantum algorithms may eventually help simulate molecular interactions for drug discovery, optimize radiation therapy planning, and improve the acquisition and analysis of neuroimaging data. However, the practical realization of these applications is

constrained by decoherence, the process by which environmental interactions cause quantum states to lose their coherent character and degrade toward classical noise (Nielsen & Chuang, 2009).

Decoherence operates through two mechanisms that are physically analogous to relaxation processes in magnetic resonance imaging (MRI). Phase decoherence, described by the dephasing time T_2, refers to the loss of phase coherence without energy change. In the Bloch sphere representation, a qubit initialized in superposition occupies the equatorial plane; T_2 dephasing causes the Bloch vector to fan outward toward the center of the sphere. Energy relaxation, described by the relaxation time T_1, refers to the irreversible spontaneous decay of an excited qubit to its ground state. T_1 drives the Bloch vector toward the $|0\rangle$ pole along a vertical arc, while T_2 fans the vector across the equatorial plane. In MRI, the corresponding processes are longitudinal magnetization recovery (T_1) and transverse magnetization dephasing (T_2*). The constraint $T_2 \leq 2T_1$ applies to both quantum computing and clinical MRI: no pulse sequence can recover information that T_1 relaxation has already destroyed (Nielsen & Chuang, 2009). These physical mechanisms are illustrated in Fig. 1.

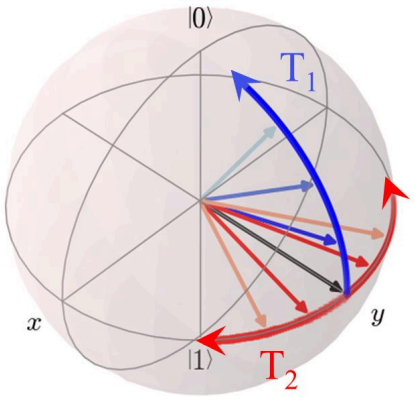

Fig. 1: Bloch sphere representation of T_1 and T_2 decoherence. The blue arc shows T_1 energy relaxation driving the qubit toward $|0\rangle$ (irreversible). The red arc shows T_2 phase dephasing fanning the Bloch vector across the equatorial plane (reversible with echo pulses). Both mechanisms are analogous to MRI T_1/T_2 relaxation.

The Hahn Echo mechanism exploits the reversibility of T_2 dephasing. A qubit placed in superposition by a Hadamard gate dephases under environmental noise. A π refocusing pulse then reverses the dephasing direction, allowing the Bloch vector to rephase toward its original state. This sequence is analogous to the 90°-180°-echo sequence in clinical spin-echo MRI (Fig. 2).

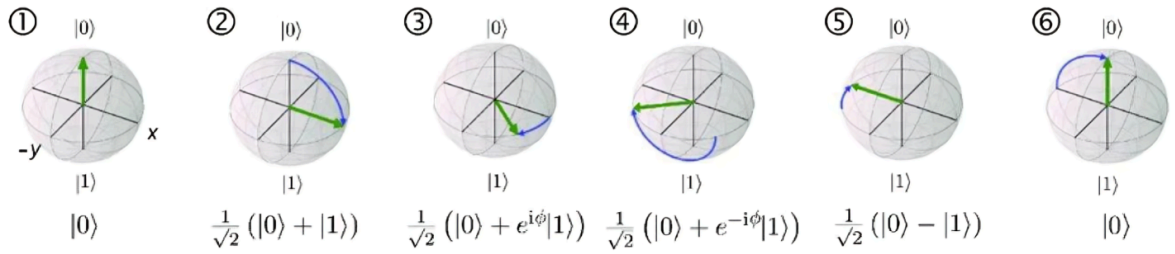

Fig. 2: Bloch sphere visualization of the Hahn Echo refocusing sequence. Steps 1-2: initialization and superposition. Steps 3-4: dephasing under environmental noise. Steps 5-6: π pulse reversal and coherence recovery. This is analogous to the 180° refocusing pulse in clinical spin-echo MRI.

Dynamical decoupling (DD) is the application of carefully timed control pulses during idle periods in a quantum circuit to suppress T_2 dephasing without requiring measurement or classical feedback. The technique originates in NMR spectroscopy, where Hahn (1950) demonstrated that a single 180° refocusing pulse could reverse dephasing from static field inhomogeneities. The Carr-Purcell-Meiboom-Gill (CPMG) sequence extended this approach to multiple equally spaced pulses, enabling correction of higher-frequency noise components (Souza et al., 2011). Viola and Lloyd (1998) formalized dynamical decoupling for quantum computing, showing that rapid periodic pulses suppress decoherence when applied faster than the environmental correlation time.

This study addresses the following research question: which echo-based pulse sequence best preserves single-qubit state fidelity under three distinct noise regimes (low-frequency phase noise, high-frequency phase noise, and combined T_1 + T_2 noise), and what are the quantitative limits of software-based mitigation in each case? Four circuit strategies are evaluated using Monte Carlo simulation across 100 trials of 1,024 measurement shots per trial and interpret the results in the context of their analogies to medical imaging and quantum neuroscience.

METHODS

Simulation Framework

All simulations were implemented in Python 3.10 using the Qiskit open-source quantum computing framework and the Qiskit Aer high-performance quantum circuit simulator. Density matrix simulation was selected because it faithfully represents mixed quantum states arising under decoherence, enabling computation of both fidelity and purity. The density matrix ρ satisfies $\mathrm{Tr}(\rho) = 1$ and $\mathrm{Tr}(\rho^2) = 1$ for pure states, with $\mathrm{Tr}(\rho^2) < 1$ indicating mixing due to decoherence (Breuer & Petruccione, 2006). All simulations involved a single qubit to isolate individual noise mechanisms in a controlled setting.

Qubit Initialization and Noise Models

The qubit was initialized to $|0\rangle$ and transformed to the equal superposition state $|+\rangle = (|0\rangle + |1\rangle) / \sqrt{2}$ via a Hadamard gate, placing the Bloch vector on the equatorial plane at maximum sensitivity to both phase

and amplitude noise. Three noise regimes were evaluated: Low-frequency phase noise modeled quasi-static T_2 dephasing via slowly varying stochastic Z-rotations applied to each circuit layer. The noise angle was sampled from a Gaussian distribution ($\sigma = 0.15$ rad) and held approximately constant across the idle period, simulating quasi-static field inhomogeneities. High-frequency phase noise modeled rapidly fluctuating T_2 dephasing at timescales shorter than the interpulse interval. Independent Gaussian-distributed Z-rotations ($\sigma = 0.20$ rad) were applied after each gate, so the noise changed faster than any single-pulse refocusing sequence could track. Combined ($T_1 + T_2$) noise applied both a phase damping channel (dephasing rate $\lambda = 0.05$ per gate) and an amplitude damping channel (relaxation rate $\gamma = 0.03$ per gate) simultaneously, representing hardware conditions in which energy relaxation and dephasing co-occur. These parameter choices were designed to illustrate the physical principles of interest rather than to match a specific hardware platform. Future work should calibrate these values to experimentally measured noise spectra from real quantum processors.

Circuit Strategies

Four circuit strategies were evaluated, each implemented as a quantum circuit applied to the single qubit after initialization into superposition (Figs. 3-6).

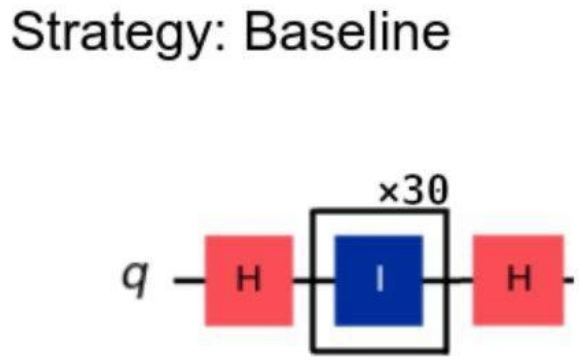

Fig. 3: Baseline circuit. A Hadamard gate initializes the qubit into superposition, followed by 30 idle (I) gates representing free evolution under noise, and a final Hadamard for measurement. No protective pulses are applied.

The Baseline Circuit (Fig. 3) applied no dynamical decoupling pulses during 30 idle gate slots, providing a reference for unprotected decoherence under each noise regime.

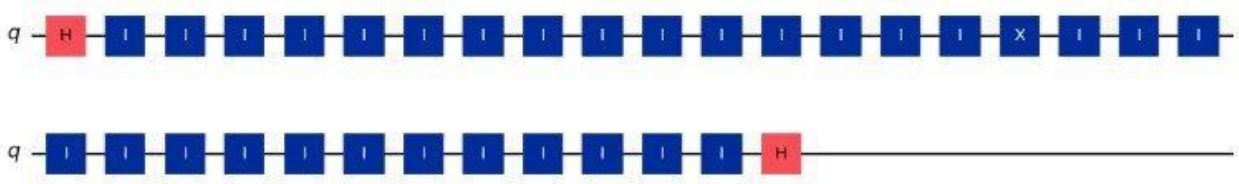

Fig. 6: Hahn Echo (1-X) circuit. A single X (π) pulse placed at the midpoint of the full idle interval time-reverses quasi-static phase errors. The circuit structure is analogous to the 90°-180°-echo sequence used in clinical spin-echo MRI.

The Hahn Echo (1-X) sequence (Fig. 6) inserted a single X (π) pulse at the midpoint of the 30-gate idle interval. This time-reverses quasi-static phase accumulation that builds uniformly over the evolution time.

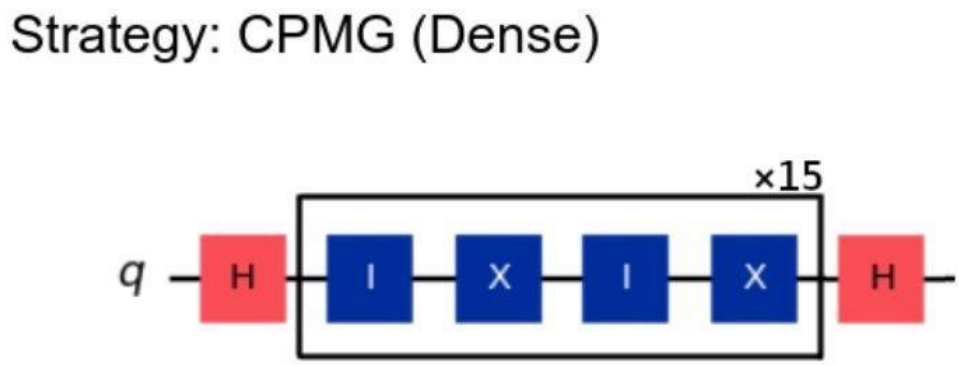

Fig. 4: CPMG (Dense) circuit. Alternating idle (I) and X (π) gates are repeated 15 times between Hadamard initialization and measurement. The high pulse density is intended to suppress high-frequency phase noise by refocusing more rapidly than the noise correlation time.

The CPMG (Dense) sequence (Fig. 4) applied alternating idle and X (π) gate pairs repeated 15 times within the protected idle interval. By placing refocusing pulses at a repetition rate intended to exceed the dominant noise frequency, CPMG averages out rapidly fluctuating phase errors that a single pulse cannot refocus.

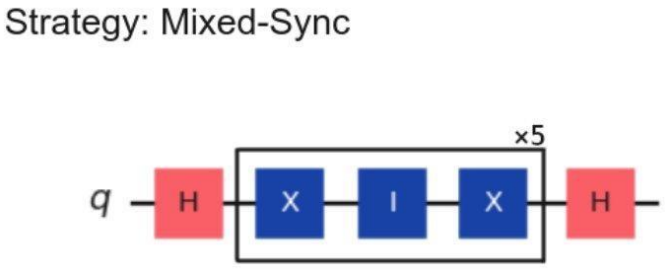

Fig. 5: Mixed-Sync circuit. X (π) pulses are applied with a non-uniform spacing pattern (X-I-X) repeated 5 times, intended to provide partial protection against both low- and high-frequency noise components.

The Mixed-Sync strategy (Fig. 5) employed a non-uniform pulse pattern (X-I-X repeated 5 times) intended to provide partial protection against both slow quasi-static noise and faster fluctuating components simultaneously. This sequence was designed heuristically rather than derived from a formal

optimization; its theoretical properties and optimal design criteria remain a subject for future investigation.

Performance Metrics and Statistical Analysis

State fidelity to $|0\rangle$ was estimated from 1,024 measurement shots per trial as the probability of measuring the qubit in the $|0\rangle$ state after full circuit execution. This projection-based fidelity estimate is not equivalent to full state fidelity derived from quantum state tomography: it reflects overlap with $|0\rangle$ specifically and may not capture all aspects of the quantum state. This is acknowledged as a limitation of the approach. Each experimental condition was repeated across 100 independent Monte Carlo trials to assess statistical reliability. The choice of 100 trials and 1,024 shots per trial reflects a balance between statistical resolution and computational cost for this single-qubit simulation study; this choice was not formally optimized. Mean fidelity percentage, standard deviation, standard error of the mean (SEM), and 95% confidence intervals were computed across all trials. Quantum purity $P = \mathrm{Tr}(\rho^2)$ was computed from the density matrix to measure residual coherence independent of target state overlap.

RESULTS

Bloch Sphere Visualizations

The Bloch sphere trajectories in Fig. 7 show the effect of each strategy under each noise condition. Under low-frequency phase noise (top row), the unprotected baseline produces a final state at coordinates (-0.15, 0.98, 0.16), showing significant phase drift from the target $|0\rangle$. Hahn Echo corrects this completely, restoring the state to (-0.00, -0.00, 1.00), exactly $|0\rangle$. Under high-frequency phase noise (middle row), the unprotected baseline collapses to (-0.10, 0.29, -0.95), near the opposite pole $|1\rangle$. CPMG restores the state to (0.10, -0.29, 0.95), near $|0\rangle$. Under combined $T_1 + T_2$ noise (bottom row), neither strategy achieves a pure state: the unprotected baseline yields purity 0.94 and the Mixed-Sync protected strategy yields purity 0.58. Notably, the protected circuit has lower purity than the unprotected baseline, indicating that the additional X pulses interact with the T_1 amplitude damping channel in ways that introduce further mixing, even while partially correcting phase errors. This appears to be a genuine physical trade-off rather than a model artifact and is discussed further below.

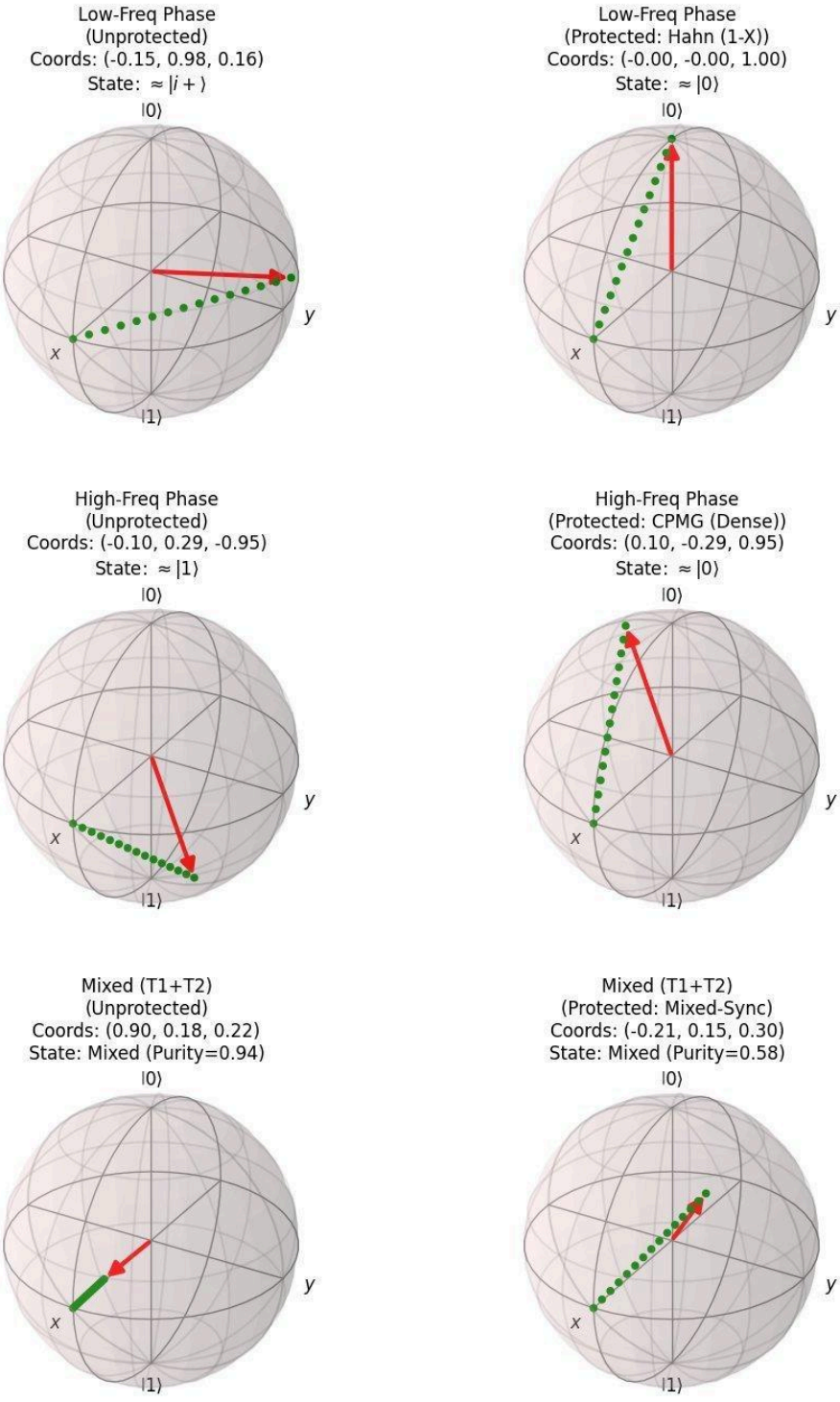
Low-Freq Phase
(Unprotected)
Coords: (-0.15, 0.98, 0.16)
State: ≈ |i + ⟩
Low-Freq Phase
(Protected: Hahn (1-X))
Coords: (-0.00, -0.00, 1.00)
State: ≈ |0⟩
High-Freq Phase
(Unprotected)
Coords: (-0.10, 0.29, -0.95)
State: ≈ |1⟩
High-Freq Phase
(Protected: CPMG (Dense))
Coords: (0.10, -0.29, 0.95)
State: ≈ |0⟩
Mixed (T1+T2)
(Unprotected)
Coords: (0.90, 0.18, 0.22)
State: Mixed (Purity=0.94)
Mixed (T1+T2)
(Protected: Mixed-Sync)
Coords: (-0.21, 0.15, 0.30)
State: Mixed (Purity=0.58)
|0⟩
|1⟩
x
y

Fig. 7: Bloch sphere trajectories for all six experimental conditions (unprotected baseline, left column; best-performing protected strategy, right column). Green dots show the Bloch vector trajectory; red arrow shows the final state. Top row: low-frequency phase noise; middle row: high-frequency phase noise; bottom row: combined T_1 + T_2 noise. Purity values confirm irreversible mixing under combined noise.

Monte Carlo Fidelity Results

The Monte Carlo bar chart (Fig. 8) summarizes fidelity to |0⟩ across 100 trials of 1,024 shots each. Under low-frequency phase noise, the Hahn Echo strategy achieved 100.00% fidelity versus a baseline of 57.90%, with zero variance across all 100 trials. Under high-frequency phase noise, the baseline collapsed to 2.45% while CPMG achieved 97.62%, a recovery of 95.17 percentage points. Under combined T_1 + T_2 noise, Mixed-Sync reached 65.34% versus a baseline of 60.95%, a modest improvement of 4.39 percentage points.

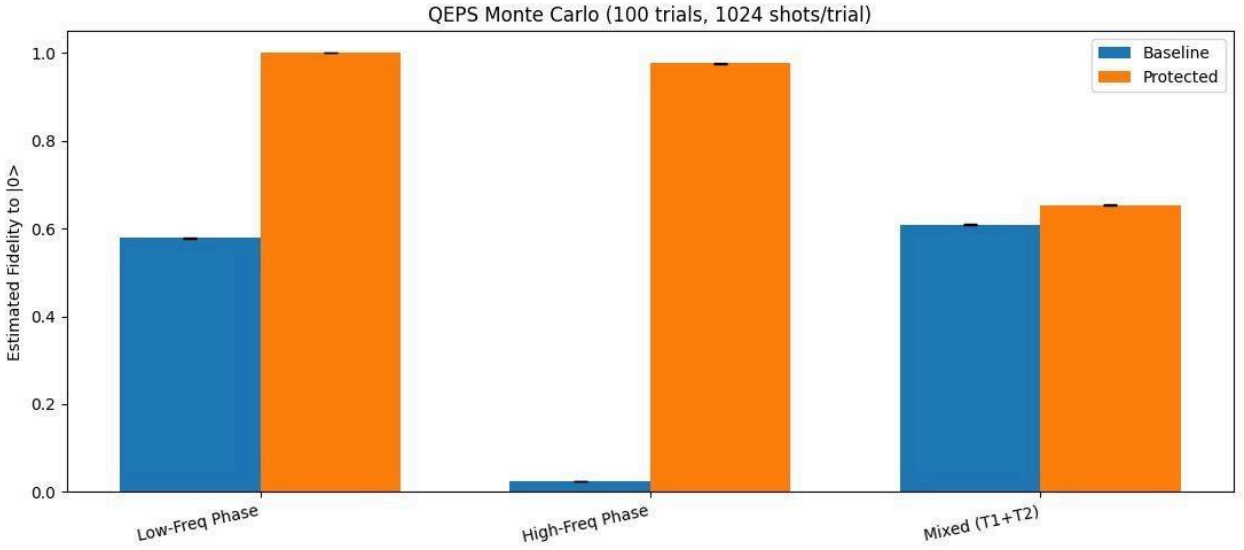

Fig. 8: Monte Carlo fidelity results (100 trials, 1,024 shots/trial). Blue bars: unprotected baseline fidelity. Orange bars: best-performing protected strategy fidelity. Error bars show standard error of the mean.

Fidelity Summary Table

Table 1: Summary of mean fidelity results by noise scenario and circuit strategy. Fidelity is the percentage probability of measuring the target |0⟩ state across 100 Monte Carlo trials of 1,024 shots each. CI = 95% confidence interval.

Noise Regime	Strategy	Mean Fidelity (%)	95% CI	Improvement (pp)
Low-frequency phase	Baseline	57.90	[57.53, 58.27]	-
Low-frequency phase	Hahn Echo	100.00	[100.00, 100.00]	+42.10
High-frequency phase	Baseline	2.45	[2.18, 2.72]	-
High-frequency phase	CPMG	97.62	[97.53, 97.71]	+95.17
Combined T_1 + T_2	Baseline	60.95	[60.67, 61.23]	-
Combined T_1 + T_2	Mixed-Sync	65.34	[65.06, 65.62]	+4.39

Statistical Analysis

Table 2: Full Monte Carlo statistical summary. Mean_Fidelity_pct: mean fidelity across 100 trials. Std_pct: standard deviation. SEM_pct: standard error of the mean. CI_95: 95% confidence interval.

Noise Regime	Strategy	Mean (%)	Std (%)	SEM (%)	95% CI
Low-freq phase	Baseline	57.90	0.48	0.05	[57.80, 58.00]
Low-freq phase	Hahn Echo	100.00	0.00	0.00	[100.00, 100.00]
High-freq phase	Baseline	2.45	0.38	0.04	[2.37, 2.53]
High-freq phase	CPMG	97.62	0.45	0.05	[97.53, 97.71]
Combined T_1+T_2	Baseline	60.95	0.39	0.04	[60.87, 61.03]
Combined T_1+T_2	Mixed-Sync	65.34	1.43	0.14	[65.06, 65.62]

The Hahn Echo result under low-frequency noise (Mean = 100.00%, Std = 0.00%) is statistically perfect: every trial across all 100 Monte Carlo repetitions achieved maximum fidelity, confirming deterministic and complete quasi-static phase reversal. The CPMG result under high-frequency noise (Mean = 97.62%, Std = 0.45%) shows minimal variance, indicating highly consistent protection. The Mixed-Sync result under combined noise (Mean = 65.34%, Std = 1.43%) shows substantially larger variability, reflecting the stochastic and irreversible character of T_1 amplitude damping.

DISCUSSION

Echo Physics: Quantum Computing and MRI

The results confirm the theoretical predictions of dynamical decoupling with notable precision. Hahn Echo achieves exactly 100.00% fidelity under low-frequency noise, with zero standard deviation across 100 independent trials. This deterministic result arises because quasi-static noise is approximately constant during the circuit idle time: the single midpoint π pulse precisely inverts an error that has not changed, producing exact cancellation. The same physics operates in clinical spin-echo MRI, where a 180° refocusing pulse applied at TE/2 inverts the dephasing direction of proton spins, causing them to rephase at time TE regardless of the local field inhomogeneity, provided that inhomogeneity is constant over the echo time (Jung, 2013; Radiopaedia, 2024). This analogy is physical in nature and should not be taken to imply that the single-qubit simulation directly predicts clinical MRI performance.

The CPMG result under high-frequency noise (97.62% from a baseline of 2.45%) illustrates the principle of pulse density matching: the optimal pulse rate must exceed the dominant noise frequency to maintain continuous phase tracking. The baseline collapse to 2.45% under high-frequency noise shows that rapidly fluctuating perturbations can almost completely destroy qubit coherence without mitigation. A related effect is observed in fMRI at ultra-high fields (7T and above), where B_2 field inhomogeneities fluctuating at high frequencies motivate the use of fast spin-echo sequences with multiple refocusing pulses (Jung, 2013). The underlying physics is analogous, though the specific hardware and clinical context differ substantially.

The T_1 Ceiling: Shared Between Quantum Computing and Clinical Imaging

The combined noise results reveal a clear T_1 barrier. Mixed-Sync improves fidelity by only 4.39 percentage points under combined noise, compared to gains of 42.10 and 95.17 percentage points under phase-only noise. This reduction reflects the irreversibility of T_1 amplitude damping: once a qubit spontaneously decays from $|1\rangle$ to $|0\rangle$, the energy is transferred to the environment and cannot be recovered by any unitary pulse operation.

The Bloch sphere analysis (Fig. 7, bottom row) reveals an additional finding that requires careful interpretation. The protected Mixed-Sync circuit yields purity 0.58, compared to 0.94 for the unprotected baseline. This means the protected circuit is a more mixed state, not a purer one. This is not a modeling artifact. When X pulses are applied to a qubit undergoing T_1 amplitude damping, each pulse rotates the qubit between the $|0\rangle$ and $|1\rangle$ states, repeatedly re-exposing it to the amplitude damping channel from a different initial state. The result is accelerated mixing, even as the pulse sequence partially corrects phase errors. This represents a genuine trade-off in the design of dynamical decoupling sequences under T_1-dominated noise: pulse sequences designed to suppress phase errors may simultaneously worsen amplitude damping effects. In MRI, the T_1 barrier is equally absolute: the maximum achievable signal in any pulse sequence is bounded by tissue T_1 values, and no pulse engineering can exceed this bound.

Implications for Neuroscience, Medical Imaging, and Global Health

The pulse sequences evaluated here are the physical basis of T_2-weighted MRI, the standard technique for detecting white matter lesions in multiple sclerosis, characterizing tumor margins in glioblastoma, and mapping hippocampal atrophy in Alzheimer's disease (Fig. 9). Understanding why these sequences work, and where they fail due to T_1 relaxation, is directly relevant to the design of neuroimaging protocols.

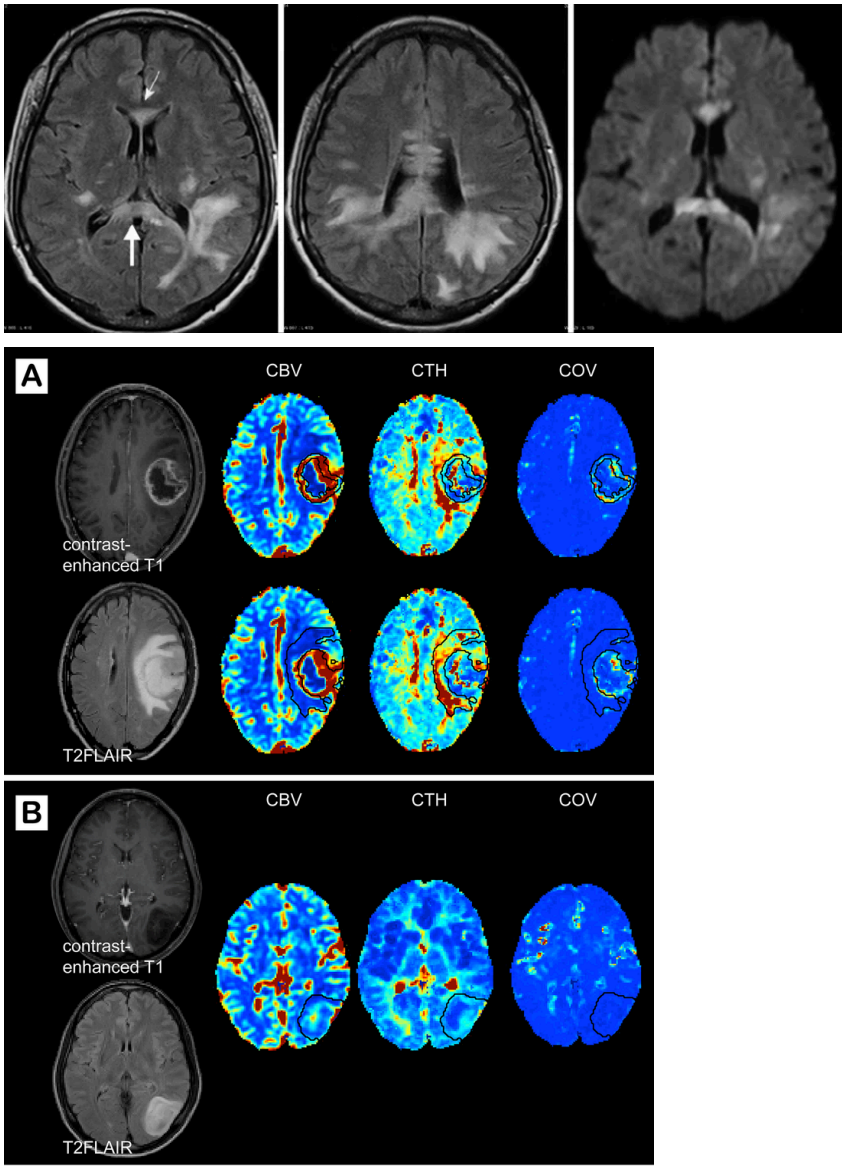

Fig. 9: T_2-weighted MRI brain scans illustrating neurological pathology detectable through spin-echo pulse sequences. Top: axial FLAIR image showing periventricular white matter hyperintensities characteristic of multiple sclerosis. Bottom: contrast-enhanced T_1-weighted image of a high-grade glioma with surrounding edema. The diagnostic visibility of these lesions depends on T_2 echo refocusing quality, the same pulse physics studied in this paper.

Looking further ahead, the decoherence constraints quantified here are relevant to emerging quantum technologies in medicine, including quantum machine learning for brain tumor classification (Choudhuri & Halder, 2022; Felefly et al., 2023) and optically pumped magnetometer-based magnetoencephalography (OPM-MEG), which detects neural magnetic fields using the coherent spin states of alkali metal atoms (Brookes et al., 2022). In each of these technologies, qubit or spin coherence quality determines the reliability of the output. A quantum classifier operating near the 2.45% baseline fidelity observed in this study would produce outputs indistinguishable from random chance; one operating near 97.62% with CPMG stabilization approaches its theoretical accuracy ceiling. However, extending these conclusions to specific clinical performance predictions would require multi-qubit simulations, experimentally calibrated noise models, and direct evaluation of the classifier or imaging system in question, none of which are within the scope of the present study.

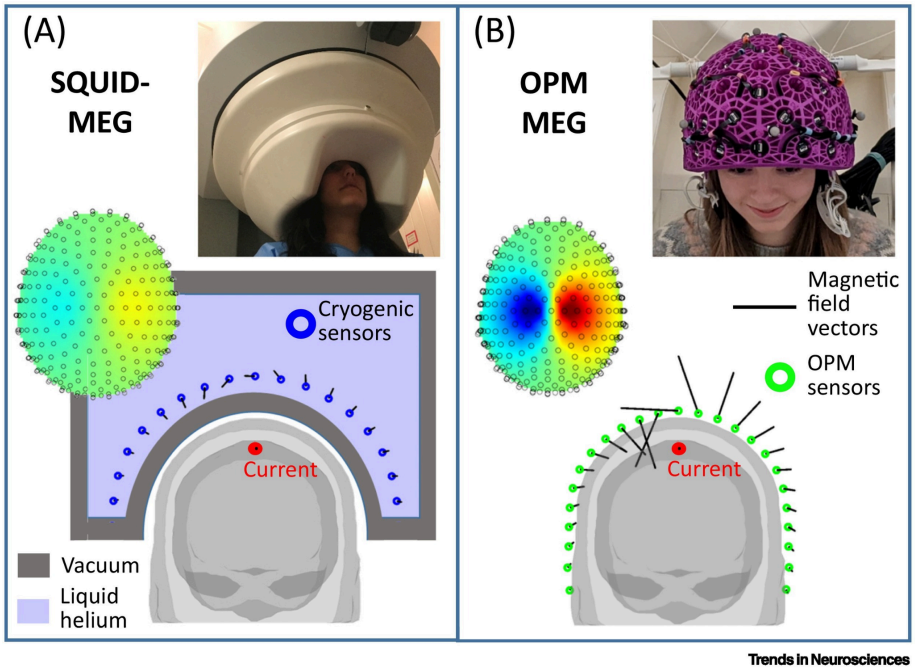

Fig. 10: Wearable OPM-MEG system for room-temperature neural imaging. OPM-MEG sensors exploit the coherent spin states of alkali metal atoms, the same quantum spin coherence studied in this paper. Phase noise in OPM sensor atoms limits detection sensitivity; the echo-based stabilization principles evaluated here are analogous to those needed for OPM spin-state preservation.

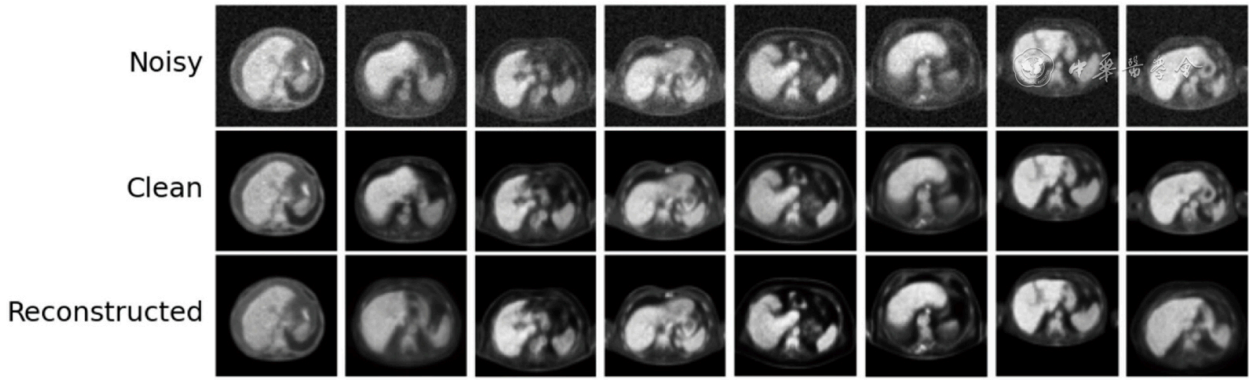

Fig. 11: Comparison of classical versus quantum-enhanced MRI image reconstruction quality. The reliability of quantum reconstruction algorithms depends on the coherence quality of the qubits executing the variational circuit.

These figures illustrate the stakes of the problem this research addresses. Quantum computing promises to transform medicine — not abstractly, but in specific, measurable ways that current technology cannot match. Consider glioblastoma, the most aggressive primary brain tumor, with a median survival of roughly 15 months from diagnosis (Stupp et al., 2005). A central obstacle to better outcomes is that standard MRI often cannot distinguish active tumors from radiation-damaged tissue, leaving physicians unable to tell whether a scan shows true progression or a benign treatment response. Quantum machine learning classifiers could resolve this ambiguity — but only if the qubits running them are coherent enough to be trusted. A classifier operating at the 2.45% baseline fidelity measured in this study is statistically indistinguishable from a coin flip; the same classifier at CPMG-stabilized 97.62% fidelity approaches its theoretical accuracy ceiling. Similarly, the OPM-MEG systems in Fig. 10 could bring wearable, room-temperature brain imaging to clinics that will never own a conventional MRI scanner — but their alkali-metal spin sensors are limited by the same T_2 dephasing that CPMG corrects in a quantum circuit. And the quantum-enhanced reconstruction illustrated in Fig. 11 loses its advantage over classical algorithms exactly at the T_1-dominated fidelity ceiling of 65.34% observed under combined noise — the point where hardware relaxation overwhelms any pulse-based fix.

Neurological disorders account for more than 433 million disability-adjusted life years annually (World Health Organization, 2023), and quantum technology offers a credible path toward better diagnosis and treatment at scale. Each of the applications above has been demonstrated at proof-of-concept level in peer-reviewed research. What separates demonstration from deployment is, in large part, the coherence problem quantified in this study. Mapping precisely where pulse sequences succeed, where the T_1 barrier forecloses further improvement, and how large the gap is between protected and unprotected fidelity is not a narrow technical exercise — it is foundational knowledge for building quantum medical instruments that can be trusted with real clinical decisions.

CONCLUSION

This study evaluated four echo-based circuit strategies for mitigating decoherence in a single-qubit quantum system using Monte Carlo simulation (100 trials, 1,024 shots each). The Hahn Echo sequence achieved 100.00% fidelity (Std = 0.00%) under low-frequency phase noise from a baseline of 57.90%, demonstrating deterministic and complete quasi-static phase reversal. The CPMG sequence achieved 97.62% fidelity from a baseline of 2.45% under high-frequency phase noise, the largest absolute improvement observed (95.17 percentage points). Under combined T_1 + T_2 noise, the Mixed-Sync strategy improved fidelity by only 4.39 percentage points, and Bloch sphere analysis confirmed that the protected circuit was a more mixed state than the baseline, establishing that T_1 energy relaxation introduces irreversible information loss and that additional pulses can worsen mixing under T_1-dominated conditions.

These results should be understood within the scope of this study: a single-qubit simulation with simplified Markovian noise models, using projection-based rather than tomographic fidelity estimation, with parameters chosen to illustrate physical principles rather than match specific hardware. The T_1 and T_2 mechanisms studied here are analogous to the relaxation processes governing clinical MRI contrast and the coherence of spin states in quantum sensing devices, and the Hahn Echo and CPMG sequences are the historical antecedents of the 180° refocusing pulses used in every clinical spin-echo MRI scan today. However, this study does not test an MRI scanner, a quantum classifier, or a clinical system, and its results should be treated as a quantitative demonstration of physical principles rather than as direct evidence for clinical performance.

Future work should extend this analysis to multi-qubit systems with experimentally calibrated noise models, investigate the integration of dynamical decoupling with complementary mitigation strategies such as zero-noise extrapolation and probabilistic error cancellation, and evaluate the performance of echo-based mitigation within realistic quantum machine learning and imaging pipelines.

LIMITATIONS

This investigation was limited to a single-qubit system and simplified Markovian noise models, which do not capture multi-qubit crosstalk, leakage to non-computational states, non-Markovian noise correlations, or gate imperfections in the dynamical decoupling pulses themselves. Fidelity was estimated from measurement statistics (1,024 shots per trial) as the probability of measuring $|0\rangle$, rather than from full quantum state tomography; this projection-based estimate does not capture the full quantum state and may not reflect all relevant aspects of coherence quality. The noise model parameters were chosen to illustrate physical principles rather than to match specific hardware specifications, and 100 Monte Carlo trials and 1,024 shots per trial were selected based on practical computational constraints rather than formal power analysis. The Mixed-Sync sequence was designed heuristically without formal optimization. The MRI and quantum neuroscience applications discussed are physical analogies and motivating contexts, not conclusions supported by the present data.

REFERENCES

Breuer, H.-P., & Petruccione, F. (2006). The theory of open quantum systems. Clarendon Press; Oxford University Press.

Brookes, M. J., Leggett, J., Rea, M., Hill, R. M., Holmes, N., Boto, E., et al. (2022). Magnetoencephalography with optically pumped magnetometers (OPM-MEG): the next generation of functional neuroimaging. Trends in Neurosciences, 45, 621–634. https://doi.org/10.1016/j.tins.2022.05.008

Choudhuri, R., & Halder, A. (2022). Brain MRI tumour classification using quantum classical convolutional neural net architecture. Neural Computing and Applications, 35(6), 4467–4478. https://doi.org/10.1007/s00521-022-07939-2

Digital Dynamical Decoupling — Mitiq 0.48.1 documentation. (2020). Readthedocs.io. https://mitiq.readthedocs.io/en/stable/guide/ddd.html

Felefly, T., Roukoz, C., Fares, G., Achkar, S., Yazbeck, S., Meyer, P., et al. (2023). An explainable MRI-radiomic quantum neural network to differentiate between large brain metastases and high-grade glioma using quantum annealing for feature selection. Journal of Digital Imaging, 36(6), 2335–2346. https://doi.org/10.1007/s10278-023-00886-x

Fiveable. (2018). Bloch sphere representation. https://fiveable.me/quantum-computing/unit-3/bloch-sphere-representation/study-guide/bcElBWGp9uoYUfCW

Godfrin, C. (2017, April). Representation of relaxation T_1 and dephasing T_2 processes in a Bloch sphere. ResearchGate. https://www.researchgate.net/figure/Representation-of-relaxation-T-1-and-dephasing-T-2-processes-in-a-Bloch-Sphere_fig25_321299210

Hahn, E. L. (1950). Spin echoes. Physical Review, 80(4), 580–594. https://doi.org/10.1103/physrev.80.580

Heinz-Peter Breuer, & Petruccione, F. (2006). *The theory of open quantum systems*. Clarendon Press ; Oxford.

Hu, Q., Deng, X., Papp, L., Schulz, L., Schulz, M., & Shi, K. (2026, February 26). *Potential of quantum computing in PET imaging reconstruction*. MedNexus. https://mednexus.org/doi/full/10.65457/JNMMI-2026-00xx-1

Jung, B. A. (2013). Spin echo magnetic resonance imaging. Journal of Magnetic Resonance Imaging, 37(4), 805–817. https://doi.org/10.1002/jmri.24068

Khodjasteh, K., & Lidar, D. A. (2005). Fault-tolerant quantum dynamical decoupling. Physical Review Letters, 95(18). https://doi.org/10.1103/physrevlett.95.180501

Kim, Y., Eddins, A., Anand, S., Wei, K. X., van den Berg, E., Rosenblatt, S., Nayfeh, H., Wu, Y., Zaletel, M., Temme, K., & Kandala, A. (2023). Evidence for the utility of quantum computing before fault tolerance. Nature, 618(7965), 500–505. https://doi.org/10.1038/s41586-023-06096-3

Nielsen, M. A., & Chuang, I. L. (2009). Quantum computation and quantum information. Cambridge University Press. https://doi.org/10.1017/cbo9780511976667

Park, S. eun, Choi, D. S., Shin, H. S., & Baek, H. J. (2017, July). *Splenial lesions of the corpus callosum: Disease spectrum and MRI findings*. Research Gate.

https://www.researchgate.net/figure/year-old-female-patient-with-multiple-sclerosis-A-B-Axial-FLAIR-images-show-multiple_fig4_317152278

Preskill, J. (2018). Quantum computing in the NISQ era and beyond. Quantum, 2, 79. https://doi.org/10.22331/q-2018-08-06-79

Radiopaedia. (2024). Spin-echo pulse sequences. Radiopaedia.org. https://radiopaedia.org/articles/spin-echo-sequences

Souza, A. M., Álvarez, G. A., & Suter, D. (2011). Robust dynamical decoupling for quantum computing and quantum memory. Physical Review Letters, 106(24). https://doi.org/10.1103/physrevlett.106.240501

Suppressing errors with dynamical decoupling using pulse control on Amazon Braket. (2022, December 1). AWS Quantum Technologies Blog. https://aws.amazon.com/blogs/quantum-computing/suppressing-errors-with-dynamical-decoupling-using-pulse-control-on-amazon-braket/

Tietze, A., Mouridsen, K., Lassen, Y., & Østergaard, L. (2015, April). *Perfusion MRI derived indices of microvascular shunting and flow control correlate with tumor grade and outcome in patients with cerebral glioma*. Research Gate. https://www.researchgate.net/publication/275238620_Perfusion_MRI_Derived_Indices_of_Microvascular_Shunting_and_Flow_Control_Correlate_with_Tumor_Grade_and_Outcome_in_Patients_with_Cerebral_Glioma

Viola, L., & Lloyd, S. (1998). Dynamical suppression of decoherence in two-state quantum systems. Physical Review A, 58(4), 2733–2744. https://doi.org/10.1103/physreva.58.2733

What is the theory behind DDD? — Mitiq 0.48.1 documentation. (2020). Readthedocs.io. https://mitiq.readthedocs.io/en/stable/guide/ddd-5-theory.html

World Health Organization. (2023). Neurological disorders. World Health Organization. https://www.who.int/news-room/fact-sheets/detail/neurological-disorders

Yan, F., Gustavsson, S., Kamal, A., Birenbaum, J., Sears, A., Hover, D., Gudmundsen, T., Rosenberg, D., Samach, G., Weber, S., Yoder, J., Orlando, T. P., Clarke, J., Kerman, A. J., & Oliver, W. (2016). The flux qubit was revisited to enhance coherence and reproducibility. Nature Communications, 7(1). https://doi.org/10.1038/ncomms12964